

Nano-scale magnetic skyrmions and target states in confined geometries

David Cortés-Ortuño,^{1,*} Niklas Romming,² Marijan Beg,³ Kirsten von Bergmann,²
André Kubetzka,² Ondrej Hovorka,¹ Hans Fangohr,^{1,3} and Roland Wiesendanger²

¹*Faculty of Engineering and Physical Sciences, University of Southampton, Southampton SO17 1BJ, United Kingdom*

²*Institute of Applied Physics, University of Hamburg, Jungiusstrasse 11, D-20355 Hamburg, Germany*

³*European XFEL GmbH, Holzkoppel 4, 22869 Schenefeld, Germany*

Research on magnetic systems with broken inversion symmetry has been stimulated by the experimental proof of particle-like configurations known as skyrmions, whose non-trivial topological properties make them ideal candidates for spintronic technology. This class of materials enables Dzyaloshinskii-Moriya interactions (DMI) which favor the stabilization of chiral configurations. Recent advances in material engineering have shown that in confined geometries it is possible to stabilize skyrmionic configurations at zero field. Moreover, it has been shown that in systems based on Pd/Fe bilayers on top of Ir(111) surfaces skyrmions can be as small as a few nanometres in diameter. In this work we present scanning tunneling microscopy measurements of small Pd/Fe and Pd₂/Fe islands on Ir(111) that exhibit a variety of different spin textures, which can be reproduced using discrete spin simulations. These configurations include skyrmions and skyrmion-like states with extra spin rotations such as the target state, which have been of interest due to their promising dynamic properties. Furthermore, using simulations we analyze the stability of these skyrmionic textures as a function of island size, applied field and boundary conditions of the system. An understanding of the parameters and conditions affecting the stability of these magnetic structures in confined geometries is crucial for the development of energetically efficient and optimally sized skyrmion-based devices.

I. INTRODUCTION

Recent advances on the study and fabrication of ferromagnetic systems with broken inversion symmetry have been highly motivated by the experimental observation of topologically non-trivial and spatially localized particle-like magnetic configurations known as skyrmions. The theoretical prediction of skyrmions and skyrmion lattices in ferromagnetic materials with Dzyaloshinskii-Moriya interactions (DMI)¹⁻³ was first confirmed by Mühlbauer *et al.*⁴ and later in numerous experimental studies where non-collinear structures were observed when imaging the magnetic texture of a sample. In particular, scanning tunneling microscopy with a spin-polarized tip⁵⁻⁸ (SP-STM) has been effective for sampling, with atomic-scale resolution, the presence and structure of individual skyrmions in interfacial systems. Studies based on the SP-STM technique applied to Pd/Fe films on an Ir(111) surface, where skyrmions need to be stabilized using an external magnetic field, have shown that individual skyrmions can be created and annihilated⁶ and how their size and shape depends on the field strength.⁷ Besides skyrmions, other non-collinear structures have been experimentally observed as equilibrium states. For example, spin spirals arise as the ground state in Pd/Fe bilayers at zero field⁶ and experiments show phases where skyrmions coexist with spin spiral configurations. Furthermore, the theory predicts different symmetrical configurations similar to skyrmions with additional rotations^{9,10}, which are known in the literature as $k\pi$ -skyrmions, with $k \in \mathbb{N}$ according to the number of rotations.

A 2π -skyrmion corresponds to a particle-like configuration with two radially symmetric spin windings and is

also known in the literature as target state. Target states have been predicted by theory^{9,10} and observed in micro-magnetic¹¹⁻¹⁶ and atomistic¹⁷ simulations. It has been claimed that the dynamics of target states caused by either spin waves^{18,19}, field gradients²⁰ or spin-polarized currents^{14,16,21,22} presents some differences with that of skyrmions, such as keeping a steady motion after switching off the current. Other effects make evident their advantage over skyrmions for their manipulation in two dimensional systems, such as racetrack geometries. These include not being affected by the skyrmion Hall effect²³, because their net topological charge is zero, reaching larger velocities under currents applied perpendicular to the hosting material,^{16,22} and not exhibiting distortion under certain conditions during their motion.^{20,22} Although recent experiments have reported the observation of target states in the ferrimagnetic²⁴ Tb₂₂Fe₆₉Co₉, the Ni₈₀Fe₂₀ ferromagnet next to a topological insulator,²⁵ and the chiral magnet²⁶ FeGe, thus far no evidence has been provided for thin ferromagnetic layers next to a heavy metal, where interfacial DMI is present.

Experimental studies of chiral materials have recently focused on the analysis of skyrmionic textures in confined geometries.^{26,27} Theoretical investigations have shown that in confined geometries skyrmions and target states can be stabilized at zero field, which is of significant importance for the potential design of skyrmion-based spintronic devices.^{8,28}

A notable feature of skyrmions in interfacial Pd/Fe samples is their small size of only a few nanometers in radius, which can be an important step forward towards the miniaturization of magnetic technology. This is in contrast with skyrmions in bulk materials such as FeGe, where the helical length is about 70 nm. The same holds

for target states, which were observed in 160 nm diameter cylinders²⁶. Although the stabilization of skyrmionic textures in extended Pd/Fe bilayer samples requires the application of a magnetic field, confined geometries offer an alternative for observing these structures at zero or weak field strengths. It is important to notice that at this low field regime, spiral structures with multiple spin rotations are energetically favored over skyrmions since the DMI and exchange energies dominate over the Zeeman energy. Hence, it is important to gain an understanding of ranges of parameters where spin spirals, skyrmions and target states are stable for their potential observation in small confined interfacial systems.

In this work we show through SP-STM measurements and numerical simulations, that a variety of chiral configurations can be stabilized in small Pd/Fe/Ir(111) islands of about 20 nm in diameter. We reproduce the experimental images using simulations based on a discrete spin model. We validate the simulations of the islands by comparing the tilting of spins at the boundary with the experimental findings. Simulations show that a variety of the experimentally observed chiral configurations are accessible through a magnetic field sweep and we characterize them through their topological number. Furthermore, we show that the confinement from the islands allows the stabilization of skyrmion-like configurations, such as a target state or a 3π -skyrmion, from zero field up to a wide range of magnetic fields below 1 T.

In addition to the analysis of Pd monolayer islands on Fe/Ir(111), we show STM images of Pd double layer islands on Fe/Ir(111) with the presence of a configuration resembling a target state. In this system the environment of the islands in applied field is ferromagnetic owing to the surrounding field-polarized Pd/Fe layer. To understand the stability of skyrmions and target states under different boundary conditions we perform a systematic study of these configurations in perfectly shaped hexagonal islands under different conditions. In this context, we compute the skyrmion and target state size and energy as a function of island size, applied field and boundary condition. Moreover, we vary these parameters to calculate the ground states of the system, which reveals conditions for the stability of different $k\pi$ -skyrmion states.

As an additional proof for the stability of skyrmions and target states, we calculate the energy barrier separating a skyrmion from the uniform ordering and the barrier between a target state and a skyrmion. We compute the barriers using the Geodesic Nudged Elastic Band Method (GNEBM)²⁹ which has been previously used to compute transitions with the least energy cost between equilibrium configurations in finite chiral systems.^{17,30-32} Our results show that the stability of target states benefits from ferromagnetic boundaries, in agreement with our experimental findings.

We start this paper by introducing in Sec. II results obtained with SP-STM measurements on the Pd monolayer on Fe/Ir(111) islands together with the theoretical basis for the simulation of these systems. Consequently,

in Sec. II B we show discrete spin simulations of the experimentally fabricated quasi-hexagonal hcp Pd islands on fcc Fe. Using different initial states we reproduce the field sweep experiment in these islands in Sec. II C. In Sec. III we discuss additional experiments performed on Pd islands on an extended Pd/Fe film on Ir(111) and simulations of these samples with ferromagnetic boundary conditions. To obtain an understanding of the experimental observation of magnetic orderings resembling a target state in the Pd₂/Fe islands, in Sec. IV we model perfectly hexagonal islands and study the energy and size of skyrmions and target states as a function of hexagon size, applied field and boundary conditions. In addition, we characterize the ground states with a full phase diagram of the hexagon system in Sec. IV B. Finally, in Sec. IV C we study the stability of skyrmions and target states by means of energy barrier and energy path calculations with the GNEBM.

II. MAGNETIC STATES IN PD/FE/IR(111) ISLANDS

A. Experimentally observed magnetic states

Spin-polarized scanning tunneling microscopy (SP-STM) is a valuable tool to study nano-scale magnetism in model-type systems.³³ Figure 1 shows spin-resolved maps of the differential conductance (left columns) of a monolayer thick hcp-stacked Pd island on an extended fcc-Fe monolayer on Ir(111) at different applied out-of-plane magnetic fields as indicated (cf. Supplemental Material, Sec. S1, for sample preparation). The presented data is obtained at a bias voltage of $U = +610$ mV and the observed signal changes within the roughly hexagonal island are due to a combination of tunnel magnetoresistance and non-collinear magnetoresistance^{33,34} (cf. Supplemental Material Sec. S2 for more details). The Pd-covered Fe (Pd/Fe bilayer) behaves as one magnetic entity and exhibits a spin spiral ground state at zero magnetic field, as evident from the stripes observed in the differential conductance map in (a).⁶

The investigated hexagonal island has a circumradius of about 9.7 nm (see (p)) and the zero magnetic field spin spiral period is about 6 nm. This spiral adjusts to the shape of the island by bending the stripes to be more perpendicular to the island edges, see (a). When a magnetic field is applied, the sample magnetization changes and at intermediate magnetic fields we observe a skyrmion next to a 360° wall, whereas at larger magnetic fields only skyrmions are observed, see Fig. 1(b)-(h). Because of the injection of higher energy electrons at the used bias voltage the tunnel current can induce changes in the sample magnetization, compare (f) and (g), which are measured at the same applied magnetic field but one skyrmion has appeared between the two measurements. At 4 T the sample reaches a uniform magnetization, see Fig. 1(i). When the applied magnetic field is reduced

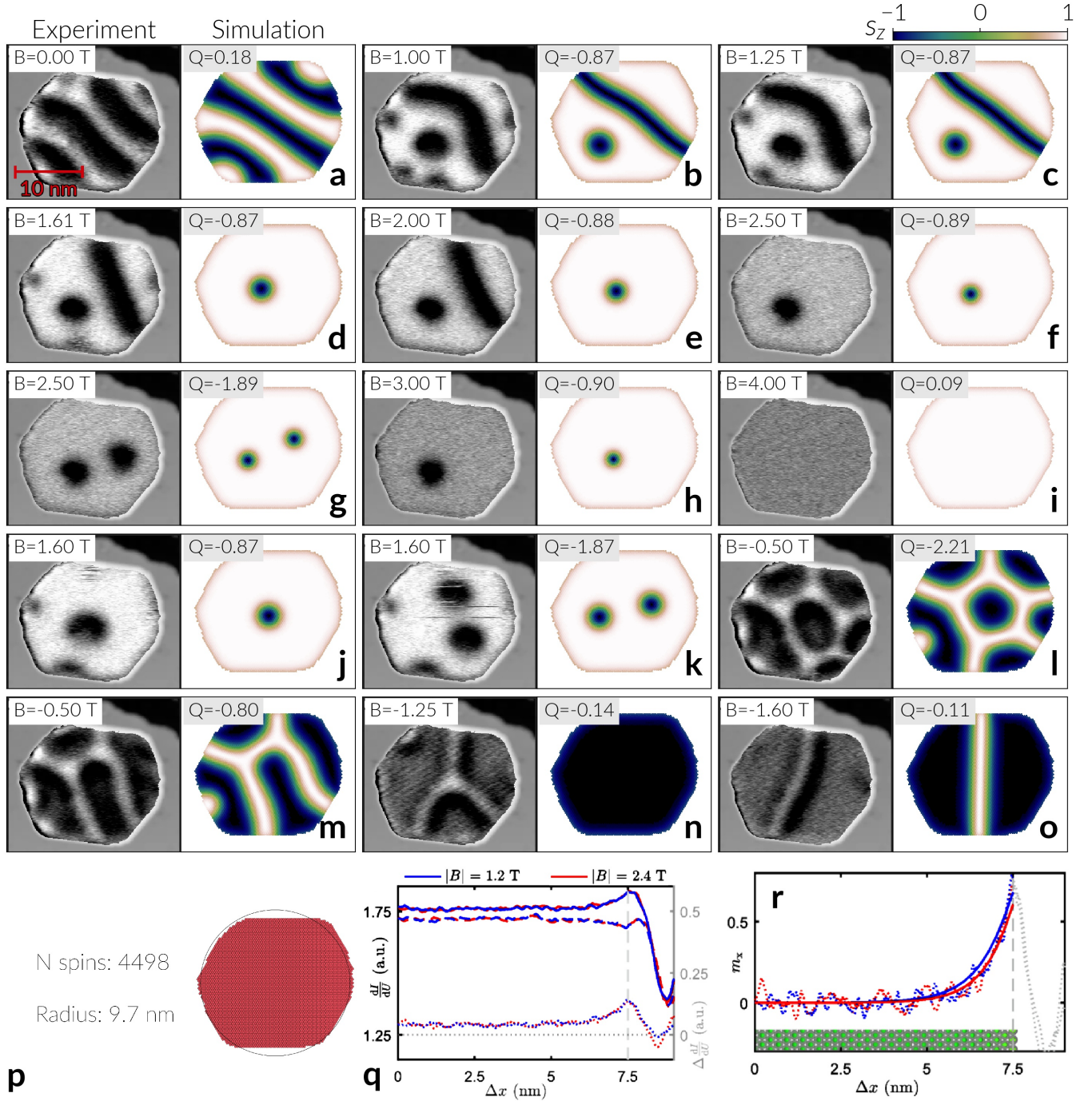


FIG. 1. Magnetic states of a roughly hexagonal hcp-Pd island on fcc-Fe/Ir(111) during a magnetic field sweep. (a)-(o) Left images: spin-resolved differential conductance maps of a hexagonal Pd/Fe island measured with a Cr-bulk tip, bias voltage $U = +610$ mV, the applied out-of-plane magnetic field B is indicated; the image is composed of the differential conductance of the island together with the surrounding topography data. Right images: corresponding discrete spin simulations, which are obtained by relaxation of the experimentally found magnetic state using the experimentally determined material parameters, see text; the calculated topological charge Q is indicated. (p) Island shape used in the simulation. (q) Line profiles of the differential conductance near the boundary of a Pd/Fe island measured at positive (solid lines) and negative (dashed lines) magnetic fields (see Supplemental Material). Dotted lines refer to the respective difference between the line profiles taken at positive and negative fields (scale on the right axis). (r) The experimentally derived in-plane m_x components at the boundary for the two magnetic field values are shown as dotted lines together with the ones from the simulations as solid lines.

again similar magnetic states reappear, i.e. at $B = 1.6$ T one or two skyrmions are found in the island, see (j) and (k).

However, when the applied magnetic field is then increased in the opposite direction the magnetic configuration of the island is dominated by a network of 360° domain walls and their junctions, see Fig. 1(l)-(n). These states are unusual magnetic configurations and we think they arise when a magnetic field is applied to a zero-field state that is not the virgin state but a metastable remanent state. We would like to point out the central region of (l), which resembles a magnetic skyrmion with the center (dark) parallel to the applied magnetic field and the surrounding (bright ring) magnetized opposite to the applied magnetic field; this means that this skyrmion has an equivalent spin texture as the one observed in (f), but it exists here in the opposite magnetic field. When the absolute value of the applied magnetic field is increased, more and more junctions of 360° walls disappear until $B = -1.6$ T when only one 360° domain wall remains; this is a state similar to the one found when the magnetic field is applied to the virgin state, see Fig. 1(d), which shows a similar 360° domain wall next to a skyrmion.

To obtain a better understanding of the magnetic field dependent stability and topological properties of the observed magnetic states in this particular Pd/Fe island, we performed discrete spin simulations of each magnetic state at the given applied magnetic field using the Fidimag³⁵ code. We translate the quasi hexagonal experimental Pd/Fe/Ir(111) island into a spin lattice, as illustrated in Fig. 1(p). We treat the Pd/Fe bilayer as a single entity and consequently simulate a monolayer of spins in a two-dimensional hexagonal lattice with open boundaries. By setting the island in the xy plane we use the following Heisenberg-like Hamiltonian,

$$\mathcal{H} = -J \sum_{\langle i,j \rangle}^P \mathbf{s}_i \cdot \mathbf{s}_j + D \sum_{\langle i,j \rangle}^P (\mathbf{r}_{ij} \times \hat{\mathbf{z}}) \cdot [\mathbf{s}_i \times \mathbf{s}_j] - \mathcal{K} \sum_i^P (\mathbf{s}_i \cdot \hat{\mathbf{z}})^2 - \sum_i^P B_z \mu_i^{(z)}. \quad (1)$$

In Eq. 1 $\boldsymbol{\mu}_i = \mu_i \mathbf{s}_i$ is the magnetic moment of the spin at the lattice site i , \mathbf{s}_i is the corresponding spin orientation with $|\mathbf{s}_i| = 1$, P is the number of spins, which depends on the lattice constant and the size of the island, \mathcal{K} is an effective anisotropy taking into account the uniaxial anisotropy and the approximation of the dipolar interactions, D is the DMI constant that describes the interfacial DMI for this material and the last term is the Zeeman interaction for the field applied perpendicular to the sample plane.

For the hcp stacking of Pd on fcc-Fe, as in this island, the continuum magnetic parameters A , D_c , and K_{eff} (exchange stiffness, DMI, and effective uniaxial anisotropy) have been obtained from previous experiments⁷, hence we convert these values into the equivalent discrete mag-

nitudes (see Sec. S5 in the Supplemental Material for details). As in the previous work⁷ we approximate dipolar interactions into the anisotropy since in the ultrathin film limit their energy contribution become significantly small^{36,37} and it is possible to approximate them as an uniaxial anisotropy,³⁸ in particular for axisymmetric solutions (which can be proved analytically⁹). Note that if the stray field is taken explicitly as in Ref. 39 the anisotropy constant is likely to have a smaller magnitude.

The results of relaxing a particular experimentally found magnetic state at the applied magnetic field are shown in the right columns of Fig. 1. In general, the simulations are highly accurate in reproducing the magnetic configurations from the experiments at the corresponding applied fields. Discrepancies arise for the magnetic states shown in Fig. 1(d), (e) and (n). In these cases, different factors that are not considered in the theoretical model, such as the presence of defects, might be contributing to the stabilization of the experimentally observed 360° domain walls and branches.

The topological charge of each of the simulated spin textures in the Pd/Fe island can be calculated and is indicated. For magnetic states in a confined geometry, such as this Pd/Fe island, the topological charge is usually not integer due to the edge tilt of the spin texture at the boundary of the structure. Figure 1(q) shows the line profiles of the differential conductance near the edge of a Pd/Fe island at four different applied magnetic fields. The tip magnetization axis was derived from the appearance of the skyrmions in this measurement and was found to be dominantly in the surface plane. The in-plane component of the sample magnetization can be calculated from the data presented in (q) and is plotted as dotted lines for the two different absolute applied magnetic fields in (r). The solid lines in Fig. 1(r) represent the m_x -component of the respective simulated data. Although the simulations do not include a possible change of the magnetic material close to the edge due to changes of the electronic structure, the agreement with the experimental profiles is remarkable. As evident from the experimental profiles and the calculated magnetization component m_x , the DMI indeed leads to a considerable tilting of spins at open boundaries of up to $\gtrsim 30^\circ$ with respect to the surface normal. The negligible difference between the profiles at $B = 1.2$ T and $B = 2.4$ T shows the comparably small influence of the external magnetic field on the edge tilt.

Comparison between Fig. 1(c) and (d) demonstrates that a 360° domain wall does not have a topological charge. Because the absolute value of the topological charge of a skyrmion is 1, and depending on the applied magnetic field, we can conclude that for the island shown here the edge tilt contributes to the total topological charge in a small range of $0.13 - 0.09$, which confirms the weak influence of the field. Analyzing the unusual magnetic configurations found in the experiments, Fig. 1(l),(m), we find that they have a topological charge with the same sign as the external magnetic field, in con-

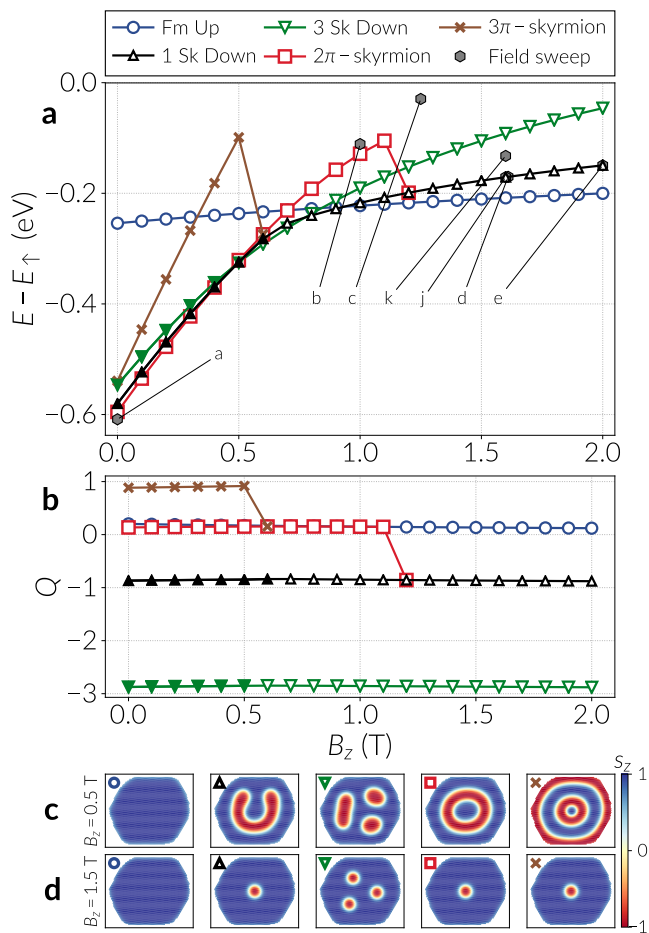


FIG. 2. Total magnetic energy and topological charge of five different magnetic configurations: ferromagnetic ordering, (FM up), a single skyrmion (1 Sk Down), three skyrmions (3 Sk Down), a target state or 2π -skyrmion, and a 3π -skyrmion. Snapshots of these states under a field of $B_z = 0.5$ T and $B_z = 1.5$ T are shown at the two bottom rows of the figure, where the color scale refers to the out-of-plane spin component s_z . Every plot is shown as a function of the applied magnetic field, which points in the z direction of the sample. (a) Total energy computed with respect to a fully saturated state (denoted by \uparrow) at corresponding magnetic field strengths. (b) Topological charge. (c)-(d) Snapshots of the configurations at two different field values indicated at the left of every row.

trast to the typical skyrmion states (*e.g.* (f)) where the topological charge and magnetic field have opposite signs.

B. Simulations of magnetic states in the island

To compare the experimentally observed magnetic states with other possible magnetic states we analyze the energy and topological charge of different simulated magnetic structures. For these simulations we define five different initial states and relax them using the Landau-Lifshitz-Gilbert equation at different magnetic fields, see

Fig. 2: a uniform ordering (\bullet) with edge tilt, a single skyrmion (\blacktriangle), three skyrmions (\blacktriangledown), a target state (\blacksquare), or 2π -skyrmion (\times), which is a target state with an extra rotation of the spins. At the bottom of Fig. 2 we show relaxed states of the five configurations at applied fields of $B_z = 0.5$ T and 1.5 T. They do not look the same for both fields because lower energy states can be found during relaxation or some of the configurations are unstable in specific ranges of the applied magnetic field. Note that at weak magnetic fields the skyrmions tend to occupy a larger area and are deformed because of the inter-skyrmion force and the boundary repulsion.

The energies of the magnetic states (Fig. 2a) are calculated with respect to the energy of a completely uniform configuration where spins point in the $+z$ direction and that we denote by \uparrow . Therefore, the energy curve labelled as Fm Up resembles the energy gain of the edge tilt. The ground state of the system for magnetic fields close to zero is likely to be a spiral with multiple rotations, since after analyzing the energy of different variations of spirals obtained from the simulations we found that they usually have lower energy than the five configurations shown. We do not show the spirals here since they are not easily classifiable. With increasing fields the Zeeman interaction becomes predominant and these spirals are not energetically favored anymore.

We can distinguish some of the configurations by their topological charge, which we show in Fig. 2b. These values are not integers due to the tilting of the spins at the boundaries. For domains magnetized out-of-plane and enclosed by a 180° domain wall, such as a skyrmion, there is associated a topological charge of one. We find that the FM state, the single skyrmion, and three skyrmions do not change their topological number in the entire magnetic field range, whereas the 2π -skyrmion and the 3π -skyrmion have a smaller stability range and decay into other magnetic states: the 3π -skyrmion state changes at $B_z = 0.6$ T to a 2π -skyrmion state, and the 2π -skyrmion state changes at $B_z = 1.2$ T to a single skyrmion state.

At weak fields, below 0.7 T, a single skyrmion becomes a worm-like domain, as shown in the second image from the left in Fig. 2c. We mark these worm domains by filled data symbols in Fig. 2a and b (*i.e.* a filled black triangle, instead of a hollow black triangle). A transition of such a worm-like domain into a circular domain exists for $B_z \geq 0.5$ T and $B_z \leq 0.7$ T (Fig. S5 in the Supplemental Material shows both configurations). This is confirmed by analyzing the energy of the magnetic interactions involved, which are shown in Sec. S6 of the Supplemental Material. The worm domain is only found by relaxing the system with a very strict (*i.e.* small) numerical tolerance of the algorithm (see simulation details in Supplemental Material, Sec. S7). For weaker (*i.e.* numerically greater) tolerances we observe that the skyrmion relaxes to a circular bubble-like domain. We see in Fig. 2a that close to a field of $B_z = 0.8$ T a single skyrmion (which is observed above $B_z = 0.5$ T) has lower energy than three skyrmions

in the sample, partially due to the Zeeman energy which is smaller for a larger ferromagnetic environment in the direction of the applied field. Furthermore, above a field of $B_z = 0.8$ T a single skyrmion and three skyrmions start having larger energy than the uniform configuration. In the case of three skyrmions, it is still possible to observe worm domains, however their presence depend on the available space in the island. This can be seen from Fig. 2c, where only one of the skyrmions is deformed into an elongated domain at weak fields. This also affects the energy of the system, where the transition occurs at fields from 0.5 T up to 0.6 T. Three skyrmion states with a worm domain are also indicated with filled data points in Fig. 2a and b.

Two other physically interesting states are the 2π and 3π skyrmions. For the latter there is still no experimental evidence in the literature. In the hexagonal islands we obtained these multiple-rotation states defining the direction of their inner core in the $+z$ direction, which follows the applied field orientation. Referring to Fig. 2a, the 2π and 3π -skyrmion states are only stable in a small range of field magnitudes. Specifically, starting from zero applied field, the 2π -skyrmion is observed up to a field of $B_z = 1.1$ T and then the system relaxes to a skyrmion for larger field magnitudes, which is evident from the topological charge in Fig. 2b. For the case of the 3π -skyrmion, it is visible even in a smaller range, only up to a field of $B_z = 0.5$ T, and afterwards it relaxes to the target and skyrmion states (this value slightly depends on the tolerance of the relaxation, weak tolerance allows to stabilize a metastable target state in a small range above 0.5 T). It is noteworthy that, for low fields, the multiple spin rotations of the 2π -skyrmion together with a large enough ferromagnetic background make this configuration the lowest energy state between the five states we are analyzing. The uniformly oriented background of spins is important because it decreases the overall exchange energy. We can explain the higher energy of the 3π -skyrmion compared to the 2π -skyrmion at fields below 0.5 T (where the 3π -skyrmion exists), by referring to the exchange and DMI energies (see Supplemental Fig. S4c and d), which are the main energy contributions. The DMI energy of the 3π -skyrmion is significantly smaller than the 2π -skyrmion, which is caused by the extra rotation of the magnetic moments, however the effect of the exchange interaction is sufficiently large to make the total energy of the 3π -skyrmion larger. This phenomenon is enhanced by the anisotropy and Zeeman energy (see Fig. S4e-f in the Supplemental Material).

In Fig. 2a we observe that target states in Pd/Fe/Ir(111) islands cannot be stabilized above a field of $B_z = 1.1$ T since the system relaxes to an isolated skyrmion. One possible reason for this instability is that the energy barrier separating these two configurations is reduced as the magnetic field increases, thus a target state would decay above a critical field. We confirmed this hypothesis by performing a stability simulation between a target state and a skyrmion by means

of the GNEBM.^{29,30} We show these results in Sec. S8 of the Supplemental Material, where we find that the critical field where the barrier goes to zero, lies between $B_z = 1.1$ T and 1.2 T.

To compare the energy of the experimentally observed configurations with the energy of the skyrmionic configurations, we show the energies of the corresponding simulated magnetic states (Fig. 1) in Fig. 2a as hexagonal markers and annotated with their corresponding letter from Fig. 1. At zero field we observe that the spin spiral (Fig. 1a) has the lowest energy, slightly below the energy of the target state. At larger fields a skyrmion coexisting with a 360° wall (Fig. 1b and c) has a higher energy compared to the other states, the single skyrmion states confirm our simulation results by lying on the corresponding curve, and, as expected, the double skyrmion energy lies between the single and triple skyrmion curves at 1.6 T.

C. Simulations of a magnetic field sweep

With the aim of devising a reproducible method to obtain the magnetic configurations observed during the field sweep experiment, we replicated this process in our simulations by starting with different initial configurations at strong fields. An adequate choice of initial states is not straightforward since it is often not possible to know every possible equilibrium state. In particular, spin spirals are difficult to specify in simulations because they can manifest as branches, i.e. long domains oriented in the $+z$ or $-z$ direction, that bend and extend in any possible direction in the island. Hence, we selected five magnetic states based on a different number of skyrmions and the configuration from experiment of Fig. 1b where a skyrmion and a 360° wall coexist next to each other. We do not show results starting from the spiral state of Fig. 1a since at sufficiently large fields it turns into a single skyrmion before saturating, and reversing the field it is not possible to obtain the spiral states from the experiments. The reason is that our simulations are performed at zero temperature and we do not consider the tunnel current from the STM tip, which can excite some of the observed states. Nevertheless, simulations show that these spiral configurations are still accessible when choosing an appropriate initial condition, as shown by the simulation of different states (Fig. 1) of the field sweep experiment discussed in Sec. II.

We set our starting point in the field sweep by relaxing these configurations at a magnetic field of $B_z = 2.5$ T, which are the states in the first row of Fig. 3. We characterize them by their topological number Q , whose absolute value effectively indicates the number of skyrmions in every snapshot. For a spin spiral $Q \approx 0$ because it only has spins rotating in a single direction. We then decrease the magnetic field in steps of -100 mT for every initial state and relax them again, repeating the process down to a field of $B_z = -2.5$ T and registering the re-

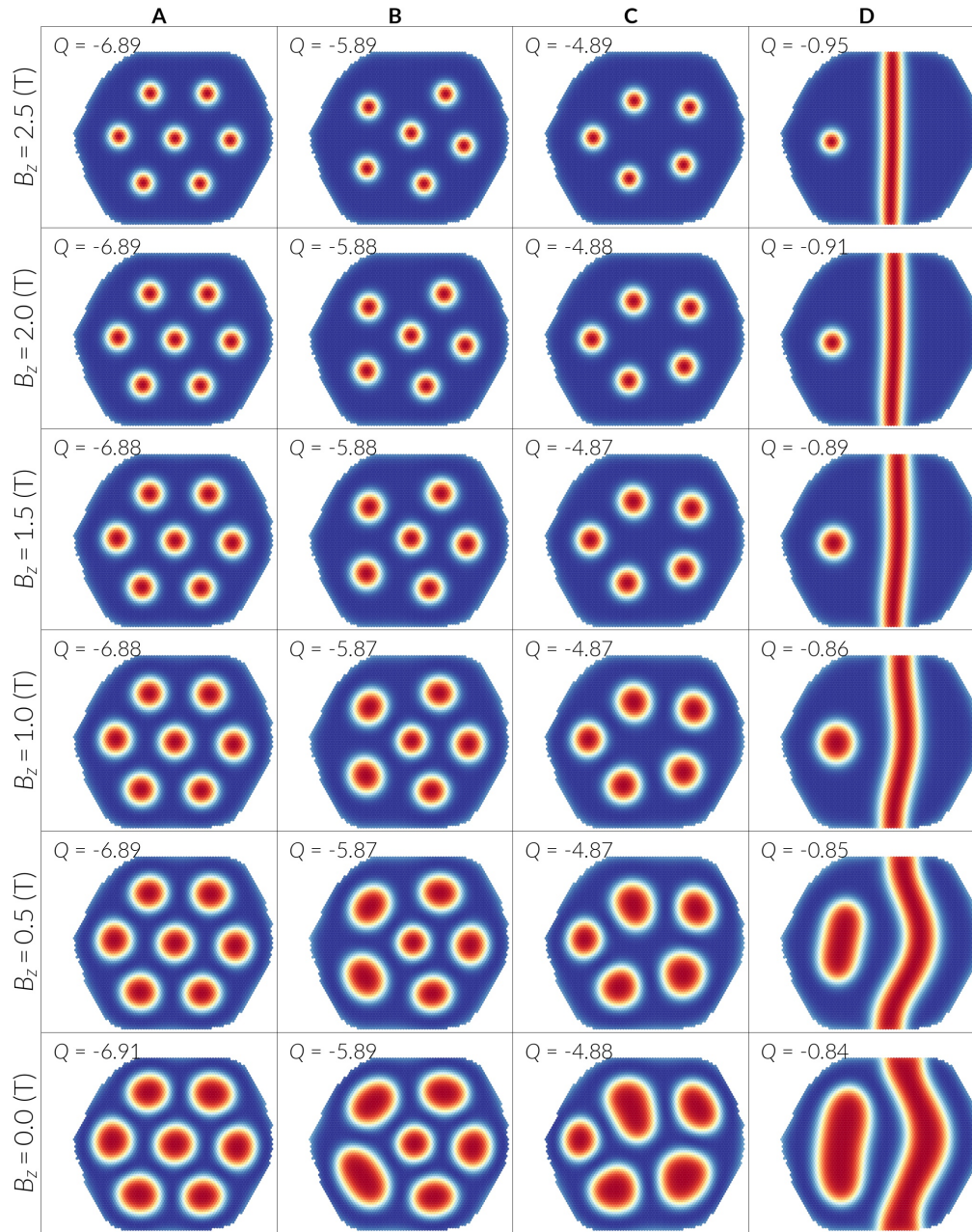


FIG. 3. Field sweep of magnetic orderings in a hexagonal island. Snapshots of magnetic configurations obtained after relaxation during a field sweep, as in a hysteresis process, with a starting field of $B_z = 2.5$ T. Columns indicate the field variation process for different initial states. The field sweep was computed in steps of 0.1 T, with this figure only showing the resulting orderings in steps of 0.5 T. The field magnitude is depicted at the left side of every row, where all the snapshots are shown at the same field value. The top left number at every snapshot plot refers to the topological charge of the system. The color scale indicates the out-of-plane component of spins which is the color scale of the snapshots in Fig. 2.

sulting configurations under equilibrium for every step. As a result, we obtain the evolution of every initial state given by the columns of Fig. 3 and 4, where we only show snapshots of the relaxed states in steps of 500 mT. We observe that as we reach zero field, skyrmions expand and occupy a larger area in the sample. When there is a large number of them, as seen in the case of column A of Fig. 3 at zero field, these configurations become more

symmetrical in shape because of the restricted available space given by the ferromagnetic background. The topological number of the different magnetic configurations changes only slightly during the magnetic field sweep to 0 T.

When the zero field is crossed, however, we observe interesting magnetic configurations which critically depend on the initial state, see Fig. 4. When we start with

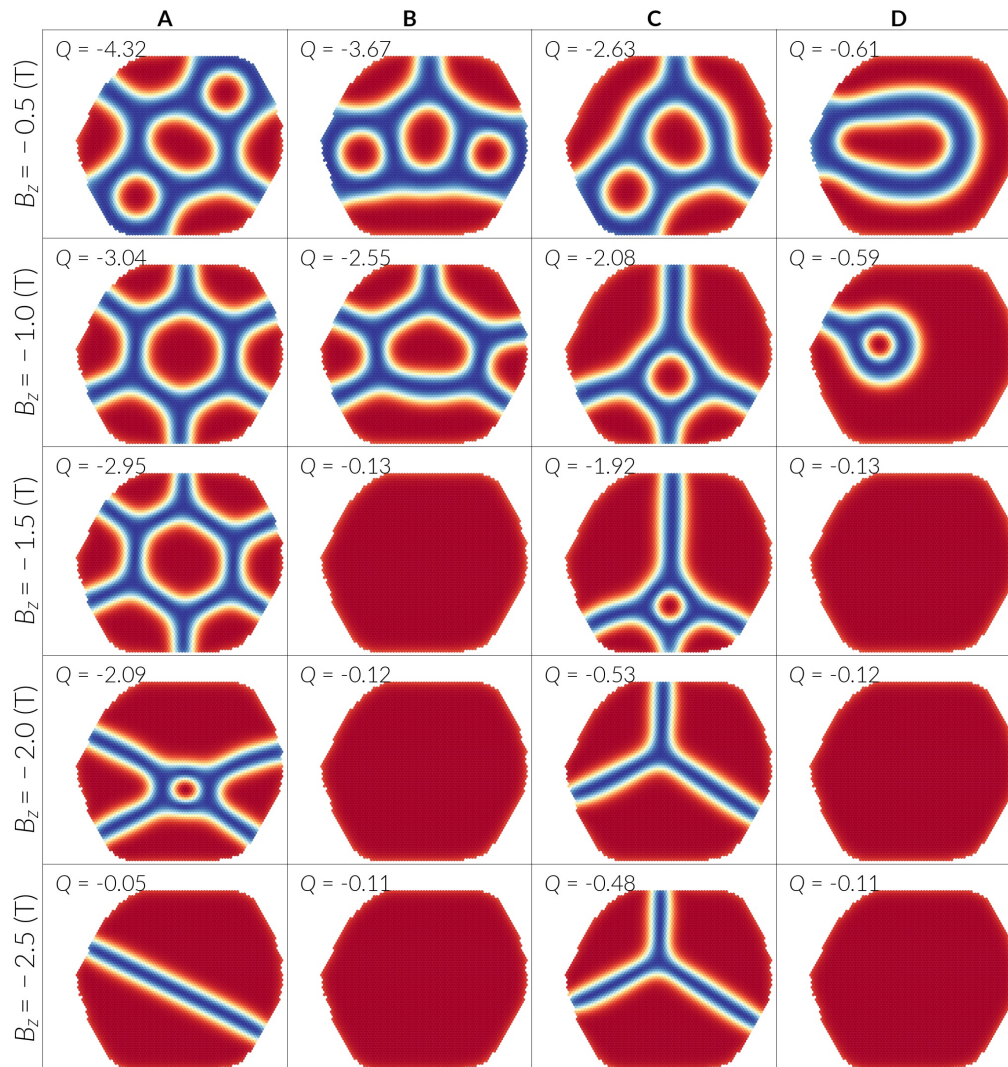


FIG. 4. Field sweep of magnetic orderings in a hexagonal island. Continuation of the field sweep process explained in Fig. 3. Field magnitudes for this case are negative and smaller than zero field, thus the field is oriented out-of-plane in the $-z$ direction.

different numbers of skyrmions we notice that domains oriented in the $-z$ direction appear surrounded by elongated domains pointing in the $+z$ direction in the form of branches whose ends tend to finish perpendicular to the hexagon sides rather than the corners, reminiscent of the magnetic states found experimentally. Indeed, they also show a topological number with the same sign as the applied field, as observed in the experimental data.

Whereas the phenomenological counting of the topological charge is rather trivial for the magnetic states shown in Fig. 3 where each skyrmion contributes a charge of one, the topological charge of the states in Fig. 4 appears less obvious at first sight. However, by carefully analyzing the magnetic states, we propose a phenomenological model to also estimate the topological charge of such unusual magnetic states. The observed enclosed domains carry a topological charge of $+1$ since their surrounding domain wall are equivalent to the skyrmion boundary.

While some of the skyrmionic structures are partially destroyed at the boundary of the island, the total number of domains in the $-z$ direction is the same as the initial number of skyrmions, which is evident from columns A-C of Fig. 4 at fields of -0.5 and -1.0 T. As expected, these incomplete skyrmionic domains do not have an integer topological charge and it is possible to roughly estimate this magnitude depending on the domain shape. Incomplete skyrmionic domains sitting in a corner at the boundary of the hexagonal island, which forms a $2\pi/3$ angle, can be identified with $|Q| \approx 1/3$ because they make a third of a full skyrmionic texture. However, when the domains are more elongated their surrounding domain walls are likely to give a small $|Q|$. Depending on the flatness of the domain walls, some of these domains can be associated with a charge of $|Q| \approx 1/6$.

For example, referring to column A of Fig. 4, at $B_z = -0.5$ T we have three skyrmionic domains which

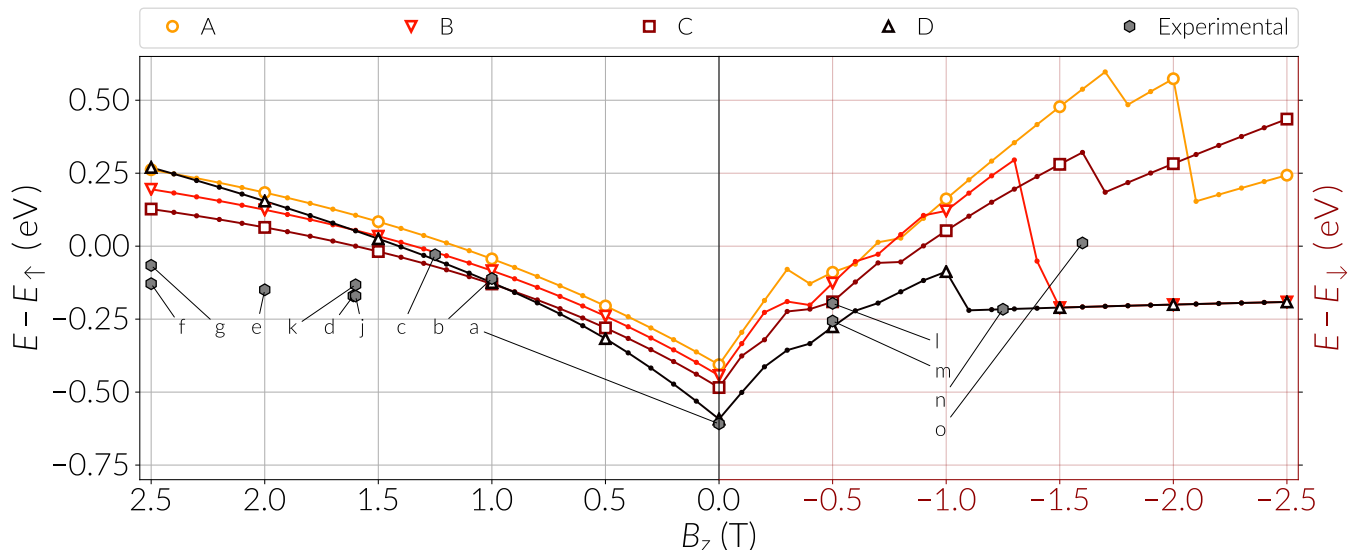


FIG. 5. Energy of the configurations in the field sweep process. At positive fields (left panel) the energy is computed relative to the energy of the fully saturated state in the z -direction, E_{\uparrow} , whereas at negative fields (right panel) the reference is the saturated state in the opposite direction E_{\downarrow} .

each contribute $|Q| = 1$ and four incomplete domains that can be identified with $|Q| \approx 1/3$, approximately summing up the total charge $|Q|$ of 4.32. Furthermore, if we now refer to the state of column C at the same field, we notice elongated boundary domains at the upper sides of the sample with a more straight profile of their surrounding domain walls, but that are not completely flat. Hence, by only considering the domain at the bottom right of the island as a third of a skyrmion, we obtain a total charge of $|Q| \approx 2 + 1/3 + 2 \times 1/6 = 2.66$, being the actual total charge $|Q| = 2.63$. Similarly, the state from column B at -1.0 T is estimated with $|Q| \approx 2.5$. In contrast, the flat profile of the domain wall from the bottom domain of the state of column B, at $B_z = -0.5$ T, makes the contribution of this domain to be zero and hence we estimate a $|Q|$ of 3.66 for the whole configuration in the island.

Another way to estimate the $|Q|$ magnitudes, is associating the triple junctions from the 360° walls with a charge of $|Q| \approx 0.5$. Hence, discarding the boundary contribution, states from the row at -1.0 T in Fig. 4 agree well with this estimation. The slight difference from the spin tilting at the boundaries can contribute up to $|Q| \approx 0.13$, as seen in column D at -1.5 T for a uniform ordering in the $-z$ direction.

To compare the energy of the states from the experimental field sweep with the configurations obtained from the simulations, we plot the energies of all the configurations as a function of the applied field in Fig. 5, where the field axis follows the order of the sweep process from left to right. Since the field orientation changes in the field sweep process, in the positive field region, shown at the left panel of Fig. 5, the energies are computed with respect to the fully saturated state energy in the $+z$ di-

rection, E_{\uparrow} . Similarly, at negative fields, we show the energy as a function of the saturated state in the opposite direction, E_{\downarrow} , in the right side of Fig. 5. Energies of the states from the experiment are shown as annotated data points with the labels according to Fig. 1. The four simulated field sweep processes are distinguished in the top legend by the column letter of Fig. 3 and 4. At the center of Fig. 5 we can see that the energy of the zero field spin spiral (data point a) is closest to the zero field state of curve D. Increasing the field, the states with a skyrmion next to a 360° wall, Fig. 1b and c, are consistent with the simulated process given by curve D. We can notice a somewhat larger energy in the experimental configurations because the orientation of the spin spiral is different in the experiment. This indicates that the spin spiral prefers to orient perpendicular to a longer or smoother edge of the island. At higher fields the experimental states, which are mainly isolated skyrmions, have a significant lower energy because the simulated configurations have larger regions of spins opposite to the field, which translates into a larger Zeeman energy cost. At negative fields, similar energies are found from the complex spiral configurations of Fig. 1l and m, with the energies of the states in curves C and D at -0.5 T. In particular, the configuration from curve D (Fig. 4 at -0.5 T) resembles Fig. 1m but with the left side of the domain shifted to the right side.

We find that the unusual magnetic states (right plot of Fig. 5) have a higher energy than the skyrmion configurations (left plot of Fig. 5), i.e. they are metastable states, which are accessible only at sufficiently low temperatures. In particular, such magnetic field sweeps at low temperature provide access to novel exotic spin textures with non-trivial topological charge. However, while

the target state is not a high energy state, it was not observed during neither the experimental nor the simulated magnetic field sweep experiments. Analyzing the resulting magnetic states one can speculate that the edge tilt and the resulting preference of 360° domain walls to be perpendicular to the edges, hinders the formation of a target state.

III. MAGNETIC STATES IN $\text{Pd}_2/\text{Fe}/\text{Ir}(111)$ ISLANDS

From simulations we will show that, in general, confinement can stabilize target skyrmions at weak fields (roughly below 0.9 T) in comparison to extended films. However, both the experiments and simulations for a nanometer-sized island of Pd/Fe on Ir(111) have not been able to produce a target state and analyzing the observed magnetic states suggests that the edge tilt at the boundary might be responsible. The Pd/Fe island is surrounded by the Fe monolayer, where a highly non-collinear nano-skyrmion lattice⁵ is present. This nano-skyrmion lattice does not change its state upon the application of an external magnetic field and has a magnetic period of about 1 nm. As this is small compared to the characteristic spin spiral wavelength of 6 – 7 nm in Pd/Fe/Ir(111), we have neglected a possible weak coupling between these layers in the simulation, treating the island edges as free boundaries.

We now turn to a different system, namely a Pd island on a Pd/Fe extended film. Our STM measurements, see Fig. 6, show, that the Pd_2/Fe island also exhibits a spin spiral state which is modified upon the application of external magnetic fields. The observed modulations on the islands are of magnetic origin, to be precise we attribute them to the non-collinear magnetoresistance effect (NCMR)³⁴, which is sensitive to changes of the local spin texture: in this case a higher signal (brighter) is observed for smaller angles between nearest neighbor spins, and a lower (darker) signal indicates larger angles between nearest neighbor spins. This means that the in-plane rotations of the spin spiral or the skyrmions appear darker, leading to two dark lines for one spin spiral period and a ring-like feature for each skyrmion (see also Supplemental Material Sec. S2).

The spin spiral wavelength is about 4.6 nm and thus slightly shorter than that of the surrounding Pd/Fe. Importantly, the transition fields to other magnetic states are much higher in the Pd_2/Fe , resulting in a situation where at about 3 T the Pd_2/Fe islands still show complex magnetic order but are surrounded by a fully field-polarized Pd/Fe film. This means that in contrast to the effectively non-magnetic environment of a Pd/Fe island, as in Fig. 1, the boundary condition in the case of a Pd island on a Pd/Fe extended film under applied magnetic field is ferromagnetic.

Figures 6(a) and (b) show the same sample area at a magnetic field of $B = +3$ T, but with a different mag-

netic field sweep history. Before the measurement shown in Fig. 6(a), the magnetic field was swept up from the virgin state at $B = 0$ T (see also Supplemental Material Sec. S4). Figure 6(b), on the contrary, is measured directly after sweeping down the magnetic field from $B = +7$ T. We observe a hysteretic behavior: during the up-sweep of the external magnetic field we find remainders of the zero-field spin spiral state (a), whereas in the down-sweep the two small islands on the right side of (b) are still in the field-polarized state and the larger islands are dominantly in the skyrmion lattice phase. In both cases small changes can be observed when the area is imaged again, see (c) and (d). We attribute the changes to either a delayed relaxation of the magnetic state towards its thermodynamic equilibrium or a non-negligible influence of the tunnel current of 1 nA with a bias voltage of $U = +50$ mV.

More significant changes are observed, after the area has been scanned with tunnel parameters of 1 nA and $U = +1$ V, see (e) and (f). The application of higher energy tunnel electrons is known to affect the magnetic state of a sample^{6,40}, which is also evident here by a comparison from Fig. 6(c) to (e), and (d) to (f). Now the large island dominantly exhibits a skyrmion lattice in both cases. In the upper right island the larger bias voltage has induced a change of the spin spiral propagation direction from (c) to (e). In the lower right island in (c) and in the case where the same two small islands on the right were in the field-polarized state (d), the tunnel electrons induced target-like states, see (e),(f).

To interpret the target-like states of the small islands in (f) we can start with the outer rim, which we assume to be dominantly parallel to the surrounding field-polarized state of the Pd/Fe extended layer, i.e. the boundary of the island is parallel to the external field. The first dark ring marks the rotation of the spins through the in-plane magnetization to the region where the spins are opposite to the applied field; note that in the upper island this dark ring is not entirely within the island but appears to be pinned to a defect at the island boundary. The second dark ring is another spin rotation through in-plane, meaning that in the center the observed target skyrmion is again parallel to the applied external magnetic field. Comparison with the magnetic states observed in the Pd/Fe island of Fig. 1 with effectively open boundary conditions suggests that the ferromagnetic surrounding is responsible for the generation and stabilization of the target state in the Pd_2/Fe islands.

IV. SKYRMION AND TARGET STATE STABILITY ANALYSIS

To enhance the general understanding on the occurrence of skyrmions and target states in the Pd/Fe and Pd_2/Fe islands we perform a systematic simulation based study of hexagons, characterized by their circumradius R , where we vary the hexagon size and the out-of-plane

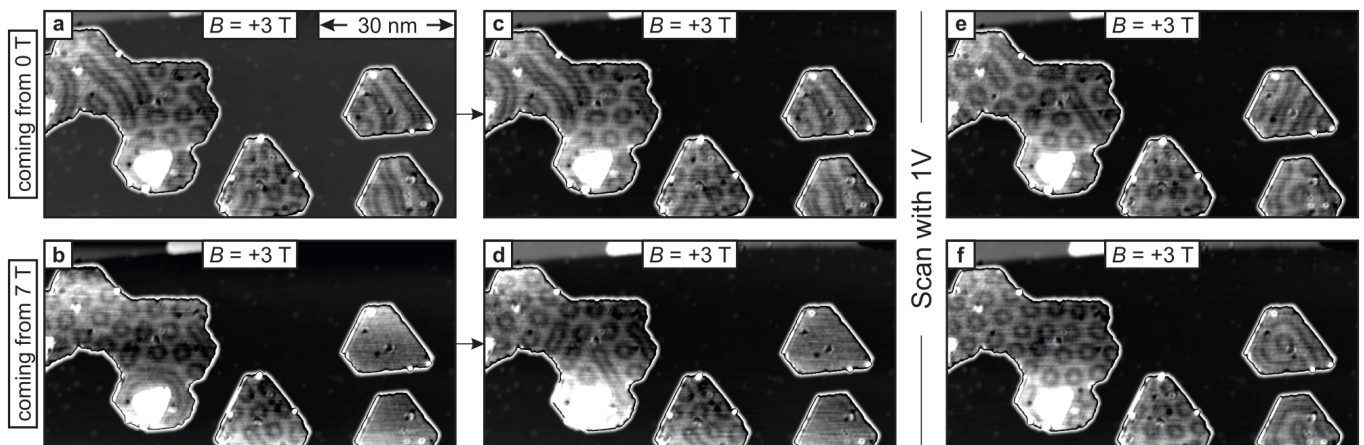


FIG. 6. Magnetic states of Pd islands on an extended Pd/Fe film on Ir(111) imaged at $B = +3$ T. STM constant-current images with the NCMR contrast on the islands adjusted locally to ± 10 pm after applying a Gauß-filter with $\sigma = 1.2$ Å in the slow scan direction, measurement parameters for all images: $U = +50$ mV, $I = 1$ nA, $T = 4.2$ K, Cr-bulk tip. (a) was obtained after a magnetic field sweep from $B = 0$ T and (b) was obtained after a magnetic field sweep from $B = +7$ T; between images (c) and (e) and between (d) and (f), the area was scanned with $U = +1$ V and $I = 3$ nA (not shown).

applied field B_z . We simulate the Pd₂/Fe islands using the same magnetic parameters as the Pd/Fe islands but changing the boundary conditions to a ferromagnetic rim, according to the discussion of Section III. In these hexagon systems we focus particularly on the effects on skyrmions and target states when tuning the three parameters R , B_z and boundary condition. The strategy we employ in these simulations is to start with either a skyrmion or a target state and relax the system with a precession-less LLG equation, as in Sec. II B.

A. Size dependence and boundary conditions

We define islands of sizes from $R = 4$ nm up to 20 nm in steps of 0.5 nm and initialize three magnetic configurations: a skyrmion profile of a radius about 1/4 of the hexagon circumradius, a target state profile of about the size of the island and a ferromagnetic configuration. We firstly compute the energy contribution from the tilted spins at the boundary of the hexagons by subtracting the energy of the fully saturated configuration (in the $+z$ direction) from the energy of the ferromagnetic state. The former is denoted by E_{\uparrow} and the latter by E_{FM} . We show this result in Fig. 7a with the energy differences as a function of the applied field. Results are shown for islands from $R = 6$ nm up to 20 nm since target states are not stable at $R = 4$ nm. We notice that the boundary energy gain with increasing fields is more pronounced for larger islands.

In Fig. 7b we calculate the energy of the skyrmion (circle markers) and target state (square markers) configurations with respect to the ferromagnetic state in islands with free boundaries. We compare this result with Fig. 7c, where we depict the energy of the two states with respect to the ferromagnetic configuration in islands with

a ferromagnetic rim. In this case of pinned-spin boundaries, the ferromagnetic state corresponds to the fully saturated state.

From the plots we observe that when ferromagnetic boundaries are present (Fig. 7c) the skyrmion has, in general, lower energy than the ferromagnetic state for fields weaker than 1.0 T. In the case of free boundaries (Fig. 7b), where the boundary spins decrease the overall energy of the system, for $R = 6$ nm there is a slight shift of the field value below which the skyrmion has larger energy than the uniform state. This effect is more pronounced for smaller R (see Supplemental Material, Sec. S10), where the skyrmion has always larger energy. We also see from Figs. 7b and c that for $R \geq 6$ nm and above $B_z = 0.6$ T, the energies of the skyrmion for different R start to get closer as the field increases. With free boundaries a small energy difference is present, however with a ferromagnetic rim this difference is unnoticeable, which means skyrmions are not influenced by the spins at the boundary. In the case of free boundaries, the influence of boundary spins vanish for sufficiently strong fields, where the skyrmion size becomes sufficiently small. In Figs. 7b and c we do not show skyrmion energies for $R \geq 10$ nm and $B_z \leq 0.6$ T because skyrmions could not be stabilized and stripe or worm domains appear as the final stable configuration.

Regarding target states, the critical field below which target states have smaller energy than the ferromagnetic state, depends more critically on the hexagon size R than in the skyrmion case owing to the steeper energy curves of target states. This dependence is more evident when free boundaries are present. Furthermore, the range of fields where boundary spins do not have an influence is smaller than in the skyrmion case. With free boundaries, at small hexagon sizes, $R \approx 6$ nm, a target state is observed up to a field of 0.5 T, whereas this critical field is

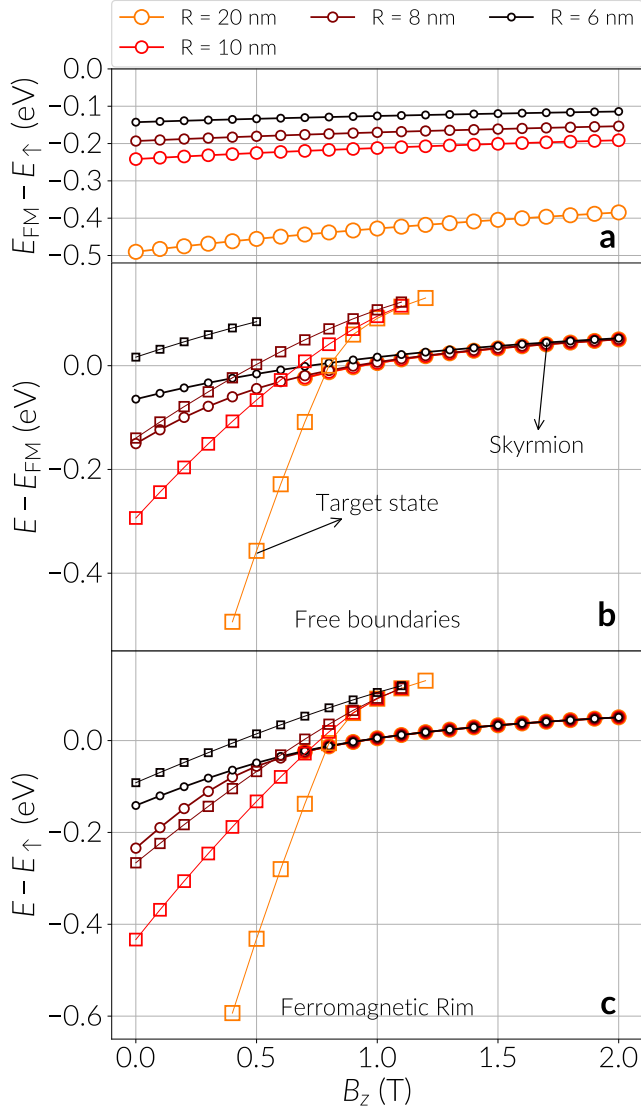


FIG. 7. Energy of the ferromagnetic boundary, skyrmion and target state in Pd/Fe/Ir(111) hexagons, as a function of the applied field for different hexagon sizes and boundary conditions. The hexagon size is defined by its circumradius R . (a) The curve refers to the energy of the ferromagnetic state E_{FM} with respect to the energy of the fully aligned configuration (in the $+z$ direction) E_{\uparrow} , as a function of the applied field. (b) Energy E of the skyrmion (circles) and target states (squares) with respect to the energy of the ferromagnetic state, as a function of the applied field. In all configurations (skyrmion, target state and ferromagnetic state), spins are tilted at the boundary. (c) Energy of the skyrmion and the target state with respect to the fully uniform configuration in an island with a ferromagnetic rim (the ferromagnetic state in this case corresponds to the fully aligned configuration).

close to the field where target states cannot be stabilized, which is around 1.2 T, when ferromagnetic boundaries are present.

A comparison of the energy of skyrmions and target states reveals that with free boundaries target states have

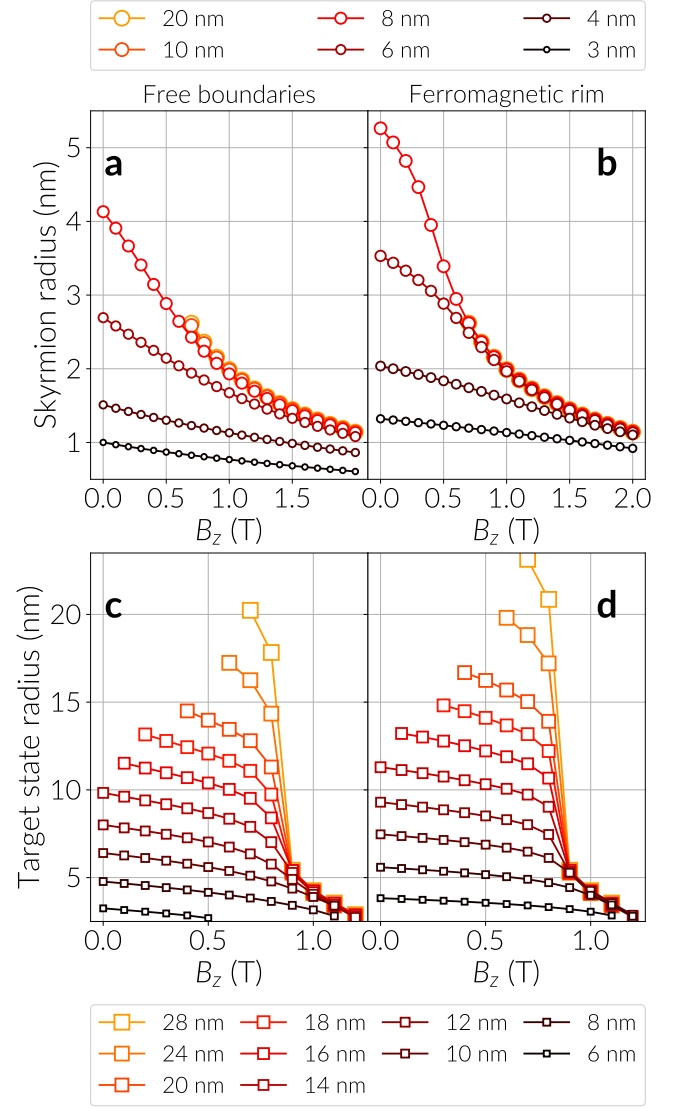


FIG. 8. Skyrmion and target state size as a function of the magnetic field and hexagon size. Hexagons are measured by their circumradius R . Skyrmion sizes are computed for hexagons with free (a) and ferromagnetic (b) boundaries. No data points are shown for $R \geq 10$ nm and weak fields since the system relaxes into a domain resembling an elongated skyrmion or into a multi-spiral state. Similarly, target state sizes in hexagons with free boundaries or a ferromagnetic rim are shown in (c) and (d), respectively. No data points are shown for $R \leq 6$ nm and sufficiently strong fields when using free boundaries because the system relaxes into a skyrmion.

always larger energy than skyrmions up to sizes around $R = 8$ nm. In contrast, with a ferromagnetic rim target states have lower energy than skyrmions at $R = 8$ nm and possibly become the ground state of the system at a critical field. Furthermore, we see that at $R \geq 10$ nm skyrmions turn into worm or stripe domains at $B_z = 0.7$ nm, however target states are stable down to zero field.

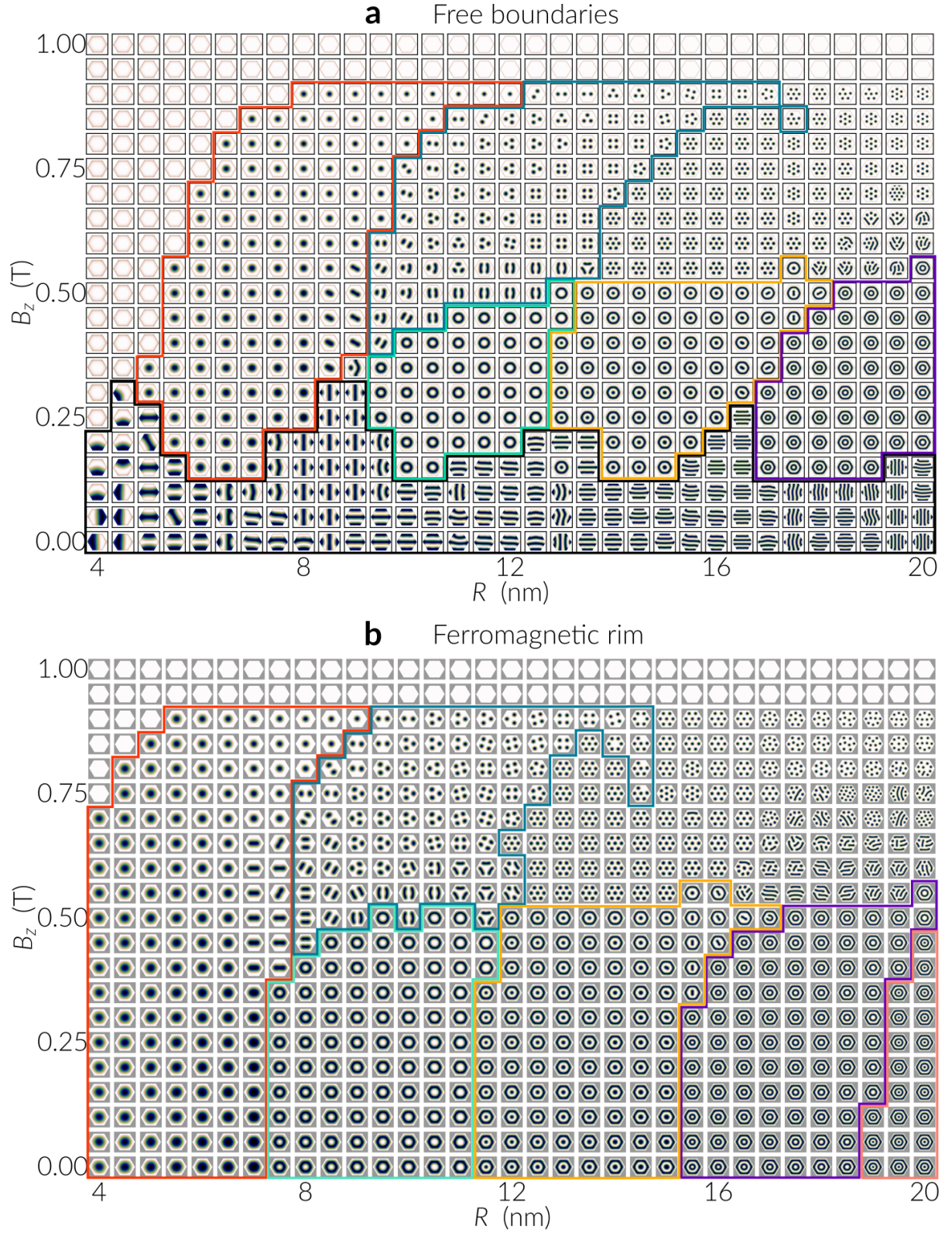


FIG. 9. Lowest energy state phase diagram of the Pd/Fe/Ir(111) and Pd₂/Fe/Ir(111) hexagon systems. The figure shows the lowest energy states of hexagon islands as a function of their circumradius R and the applied out-of-plane magnetic field B_z . Phases are marked by enclosed regions in thick lines. (a) Diagram of hexagons with open boundaries. (b) Diagram of hexagons with a ferromagnetic rim.

Similar to the behaviour of isolated skyrmions in extended systems, by increasing the magnetic field strength the skyrmion size decreases. To quantify this change we calculated the skyrmion radius as a function of the magnetic field for hexagon sizes between 3 and 20 nm and different boundary conditions. This result is depicted in Fig. 8a and b. We define the skyrmion radius as the distance, from the skyrmion center, where $m_z = 0$. In the case of $R \geq 10$ nm, the curve is not shown below certain field magnitudes since the system relaxed into elongated domains or spiral domains. For hexagon sizes below 8 nm and sufficiently small fields, we notice that skyrmions in the system with a ferromagnetic rim (Fig. 8a) are larger in size than the skyrmions in the sample with free boundaries (Fig. 8b) at equivalent field strengths and R . The reason is that for sufficiently weak applied fields the skyrmion tries to occupy the largest possible area in the island and when the island has free boundaries the tilted spins at the hexagon edges restrict the skyrmion size (see Supplemental Sec. S11), as shown in Fig. 8a. This is in contrast to the system of Fig. 8b, where pinned spins at the boundary do not limit the skyrmion and allow it to expand further towards the sample edges. When increasing the field strength skyrmions shrink, hence for sufficiently large sample size and applied field the boundary spins no longer have an influence on the skyrmion and their sizes converge to similar values regardless of the edge condition. This is in agreement with the skyrmion energy results of Fig. 7, thus we can say that confinement effects on a single skyrmion are perceived for hexagonal islands of $R \leq 10$ nm.

We define the target state radius as the outermost distance where $m_z = 0$ and we plot it as a function of hexagon size and magnetic field in Fig. 8c and d. An analysis of the radius of target states in hexagons with different boundary conditions results in the same tendency exhibited by skyrmions, i.e. target states become smaller with increasing field magnitudes and are larger in size when spins are not tilted at the sample edges. However, target states are, overall, noticeable bigger than skyrmions for hexagon radii up to 28 nm and below the critical field of 1.2 T where they become unstable. Target states can be stabilized in hexagons as small as $R = 6$ nm, where they are stable in a larger range of field magnitudes when a ferromagnetic rim is present (Fig. 8d). Below this circumradius the system relaxes to a skyrmion for the two boundary conditions. Furthermore, a critical magnetic field is observed at 0.8 T, where the size of target states in islands larger than $R > 8$ nm converges to a radius around 5 nm, and the configuration becomes small and well confined within the island. By increasing the field the radius of target states tend to a similar value, smaller than 3 nm, independent of the system size.

B. Phase diagram

As observed in the experimentally measured islands, spin spiral configurations are the most probable ground state of the system at weak fields. This is illustrated, in part, in Fig. 2, where the data point for the state from Fig. 1a has the lowest energy at zero field. At larger field values, spin spirals are no longer favored and skyrmionic textures are candidates for being the ground state. In Fig. 9 we show full phase diagrams depicting the lowest energy state of hexagons as a function of the circumradius R , the applied field and the two different boundary conditions. The lowest energy configurations were found by simulating 27 different initial states per (R, B) point in the diagram, which correspond to multiple skyrmion states up to a number of seven, $k\pi$ -skyrmion states from 2π up to 5π , random configurations, 360° domain walls and skyrmions next to a 360° wall.

The results illustrated in Fig. 9a at zero field, for hexagons with free boundaries, confirm our observations of spin spirals as ground states. By increasing the field, between $R = 5$ nm and 12 nm, at the top left enclosed region we distinguish a single skyrmion phase. Next to this region, at sufficiently large magnetic fields, we marked the area where worm domains or up to 6 multiple skyrmions become the lowest energy state. At the right of this region, a larger number of skyrmions are the lowest energy configurations. Since we specified up to seven skyrmions as initial states, it is likely that a slightly larger number of skyrmions have lower energy in this region. For example, at $R = 19$ nm and $B_z = 0.7$ T we notice a state with 12 skyrmions and 2 half-skyrmions, whose topological charge is about -12.6. Below the skyrmion regions, at lower magnetic fields and with increasing hexagon radii, target states, 3π -skyrmion and 4π -skyrmion states have the lowest energy. At fields above 0.9 T the ferromagnetic state is always the ground state. At weaker fields and when the hexagon radii are smaller than 8 nm, a region is observed where the uniform state is the lowest energy configuration because boundary spins inhibit the formation of skyrmions.

When ferromagnetic boundaries are present spin spirals are suppressed and the phases for skyrmionic textures significantly expand and are observed down to zero field, as shown in Fig. 9b. In particular, a single skyrmion becomes the ground state for islands down to 4 nm radius in size. Furthermore, because of the lack of tilted boundary spins, close to $R = 20$ nm, a phase emerges with 5π -skyrmion configurations. In agreement with the case of open boundaries, the saturation field remains at 0.9 T. In this case, the region where the uniform state is the ground state for fields below 0.9 T is smaller than in the case of open boundaries and confirms that the tilted spins at the edge hinder the formation of skyrmions in sufficiently small hexagons.

In Fig. 7 we saw that for hexagons with a radius around 8 nm, a ferromagnetic rim causes target states to have smaller energy than skyrmions for fields below 0.6 T.

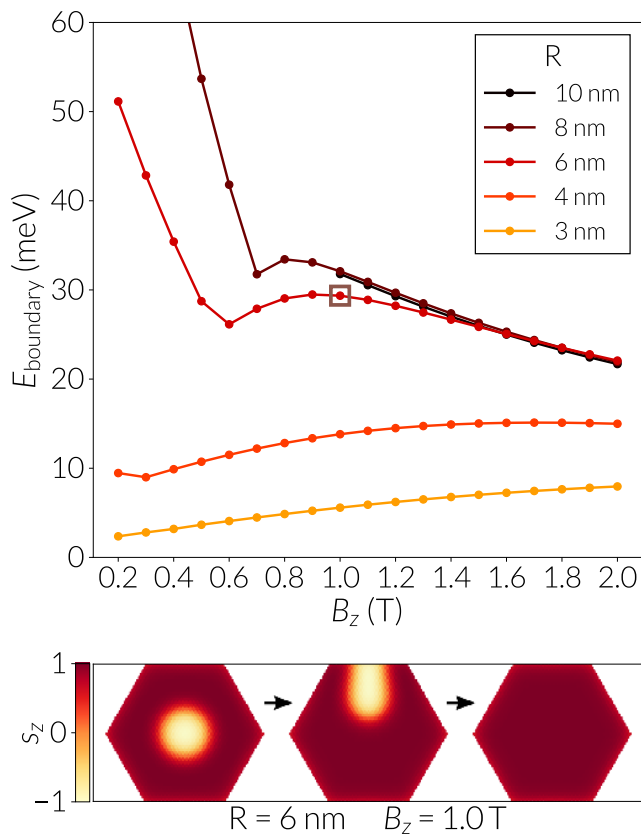


FIG. 10. Energy barrier for the skyrmion escape through the boundary of hexagons of different size. Barriers are calculated for free boundary hexagons of variable circumradius R and magnetic field strength. For $R \geq 6$ nm and weak fields the change in the tendency of the curves is because the skyrmion (which has a large size at weak fields) elongates until reaching the boundary instead of being displaced while keeping its symmetrical shape. Snapshots with the escape transition are shown below the figure for the parameters of the data point marked with an open square in the energy barrier curves.

From Fig. 9b we notice that in islands with a ferromagnetic rim the target state becomes the lowest energy state in a region of hexagon radii from approximately 7.5 nm up to 11 nm and below fields of 0.5 T, and hence it is energetically favored in this region of phase space. Furthermore, since the islands measured experimentally have a radius of about 9 nm we can infer that target states in Pd_2/Fe islands have a larger probability of being observed if the system overcomes energy barriers towards lowest energy configurations.

C. Stability of skyrmions and target states

A method for the estimation of the stability of skyrmions is the calculation of energy barriers separating them from other equilibrium states, in particular from the uniform state. Two known mechanisms^{29–32} for the

skyrmion annihilation (creation) are the skyrmion collapse (emergence) and the skyrmion escape (nucleation) mediated by the boundary. The latter is only possible when free boundaries are present.

In Fig. 10 we show the energy barriers between the skyrmion and the uniform state via the escape mechanism for the system with open boundaries. To obtain this transition, we initialized the algorithm by moving the skyrmion towards the upper boundary of the hexagon. In the figure we observe that for $R < 6$ nm the height of the barrier increases with larger field strengths, and for $R \geq 6$ nm we see the opposite tendency. Furthermore, for $R \geq 6$ nm and fields 0.6 T there is a drastic change in the slope of the curve because the skyrmion elongates towards a boundary until reaching the sample border and starts escaping, instead of displacing without deformation towards the sample edge, as occurs for sufficiently large fields. In small samples the effect is unnoticed since the skyrmion is directly touching the sample boundaries, thus it can easily transition towards the uniform state. Snapshots of these transitions for an $R = 8$ nm hexagon and energy bands from the simulations are shown in Sec. S12 of the Supplemental Material.

Regarding the collapse mechanism, we summarize the energy barrier calculations in Fig. 11, for the two boundary conditions. In this case we notice the barriers of hexagons with free boundaries (Fig. 11a) are smaller in magnitude than the corresponding barriers from the system with ferromagnetic boundaries (Fig. 11b). Additionally, in Fig. 11a at $R = 6$ nm and below $B_z = 0.5$ T the algorithm finds a different energy path, which is mediated by the boundary and is not allowed when the system has fixed spins at the boundary. The change in the curve around 0.8 T for circumradius above 6 nm indicate the collapse of the skyrmion through a singularity,³⁰ which is not present at larger magnetic fields or in small sample sizes since the singularity is defined in a few atomic spaces. For the hexagon with the ferromagnetic rim there are no effects from the boundary, however singularities still appear at sufficiently large sample or skyrmion sizes, which can be seen from the small jumps in the curves of Fig. 11b. According to these results, it is possible that the boundary has an influence on the formation of a singularity for large enough hexagons. For fields below 0.8 T and circumradius of 10 nm and above, we do not show data points since the system relaxes into an elongated skyrmionic domain or spiral domain.

An investigation of the transition energies of target states into skyrmions can provide us an alternative answer for the problem of stability of target states. We computed this transition for different hexagon sizes and boundary conditions and summarize the results in Fig. 12. From the simulations with $R \leq 8$ nm we observe that the minimum energy path is given by the collapse of the inner core of the target state, which is oriented along the field direction $+z$, making the ring of spins in the $-z$ direction to expand into the skyrmion centre (see Supplemental Fig. S13). The same mechanism has

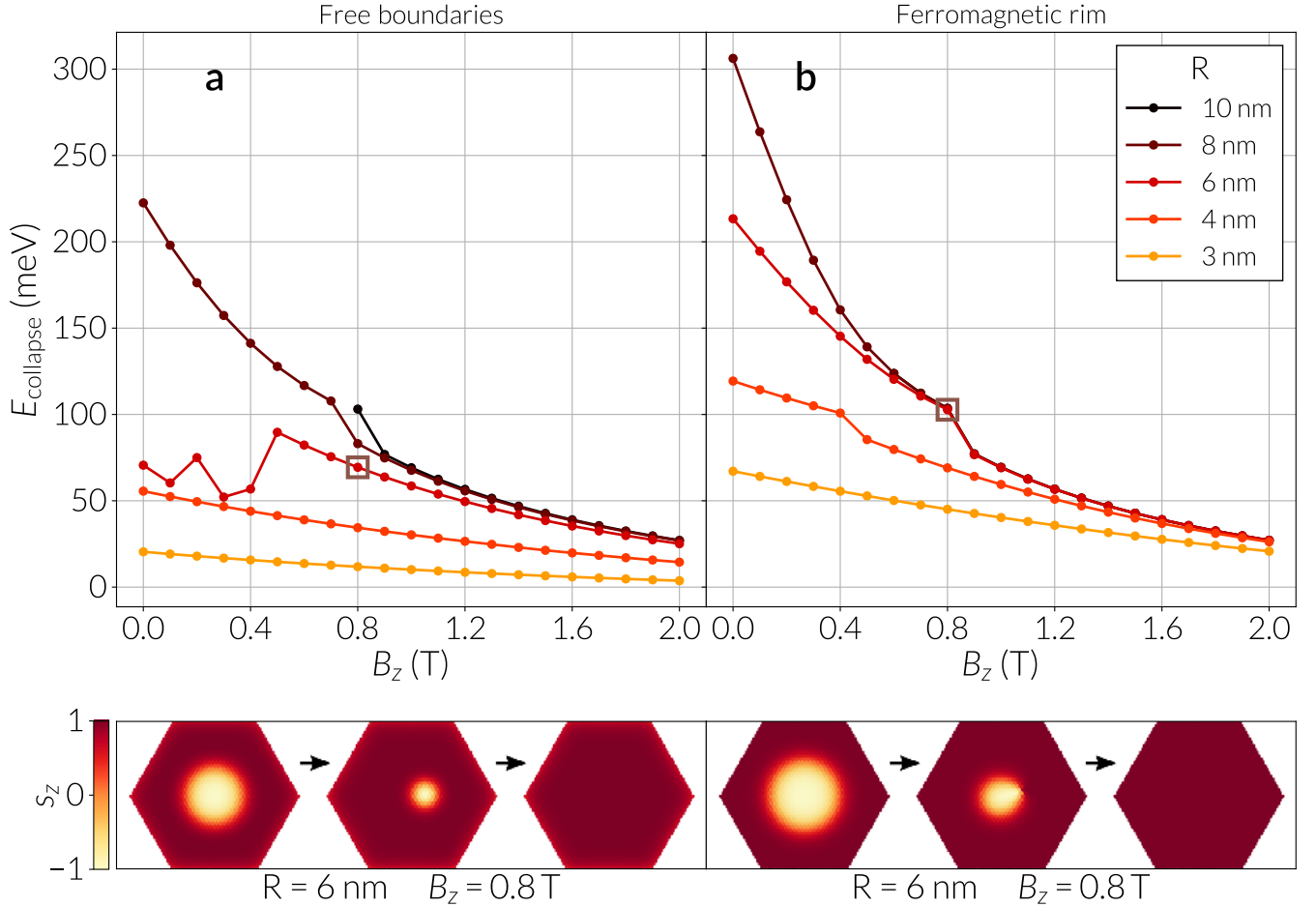


FIG. 11. Energy barrier for the skyrmion collapse in hexagons of different size. Barriers are calculated for hexagons with either free (a) or ferromagnetic (b) boundaries, and variable circumradius R and magnetic field strength. For $R = 6$ nm and weak fields, the change in the curve tendency is because the NEBM finds a boundary mediated transition rather than a collapse. For $R \leq 8$ nm and weak fields, the change in the curve is because the NEBM finds a skyrmion collapse mediated by a singularity. Snapshots with the collapse transition (below (a)) and the collapse via a singularity (below (b)) are shown below the corresponding plots with different boundary conditions and for the data points marked with open squares in the energy barrier curves.

been reported by Hagemester *et al.*¹⁷ in infinite samples. When the system has free boundaries, other possible energy paths for the target state involve the boundaries of the hexagon and during this process complex spiral orderings mediate the transition. Unfortunately, our attempts to calculate transitions from target states to either a ferromagnetic state or a skyrmion, via the boundary of the system, were not successful owing to the lack of convergence of the algorithm to a consistent result, thus a study of these paths requires a more careful analysis.

The inner collapse transitions are given by the smooth curves of Fig. 12. An exception occurs for $R \geq 8$ nm, $B \lesssim 1.0$ T and ferromagnetic boundaries (Fig. 12b), since the transition in those cases is given by the emergence of a singularity at the ring of $-z$ spins (see Supplemental Fig. S14). The reason is that the target state is larger in size when a ferromagnetic rim is present, as we saw in Fig. 8, which must be around a critical size for sin-

gularities to mediate the transition, as in the case of the skyrmion collapse. The same effect occurs for $R > 8$ nm and weak fields for the two boundary conditions, hence the algorithm did not converge to an optimal path for fields below 0.9 T. The energy barrier calculations indicate that target states have associated larger barriers to decay into the skyrmion state in hexagons with a ferromagnetic rim. Moreover, the most evident mechanism for the annihilation of a target state is through a collapse or a disruption mediated by a singularity, since boundary effects are forbidden. Although there are possibly multiple other energy paths for the annihilation of a target state, for example the transition of a target state into more than one skyrmion, they are likely to have associated larger energy barriers because multiple singularities would be necessary to mediate these transitions. These results suggest that the transition path of a target state into a single skyrmion is the shortest in energy landscape

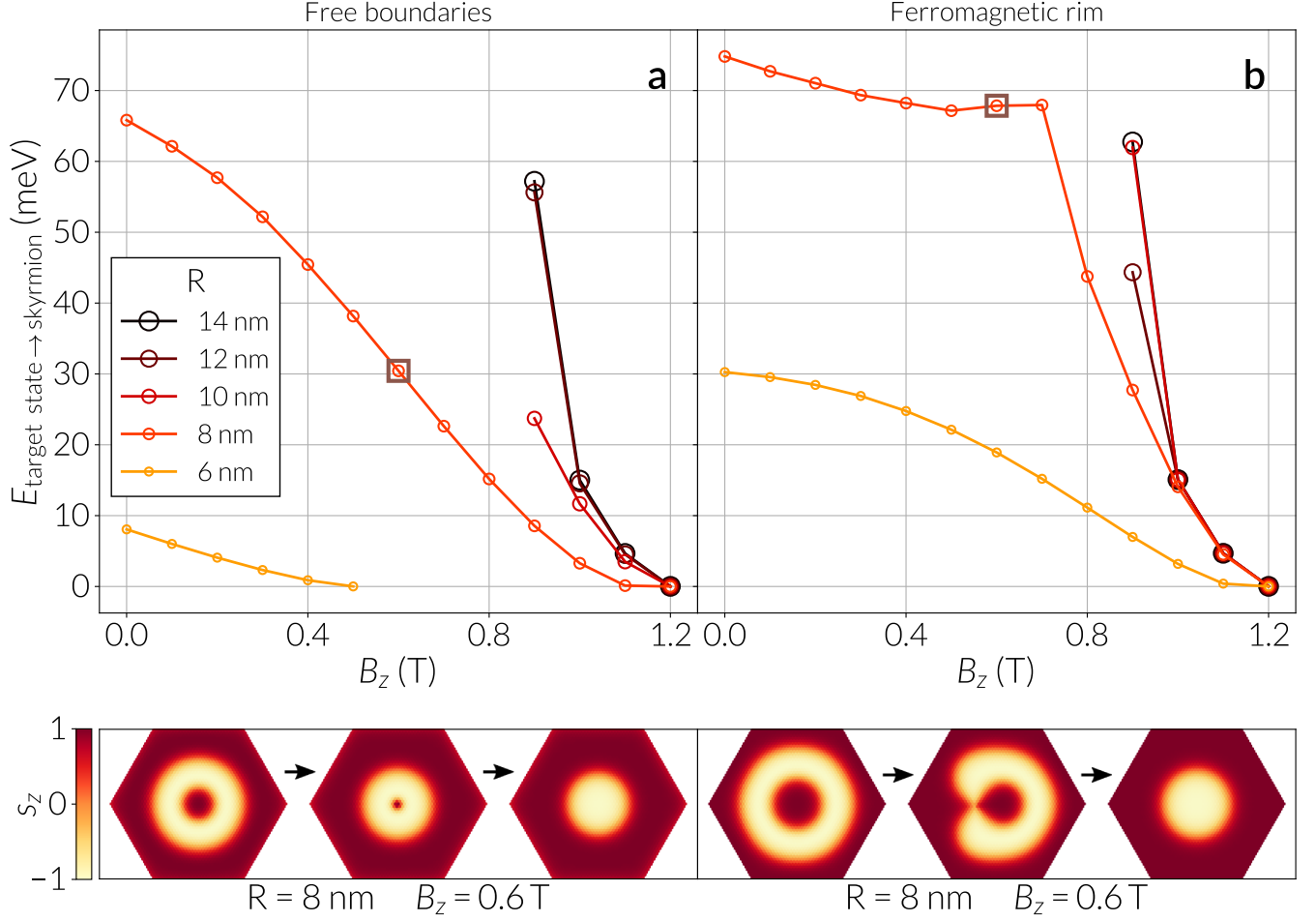


FIG. 12. Energy barrier for the transition of a target state into a skyrmion in hexagons of different size. Barriers are calculated for hexagons with either free (a) or ferromagnetic (b) boundaries, and variable circumradius R and magnetic field strength. For sufficiently large hexagon sizes the algorithm was not able to converge since transitions are mediated by singularities and the initial state used is not optimal to find a different path. Snapshots with an internal collapse of the target state (below (a)) and the transition via a singularity (below (b)) are shown below the corresponding plots with different boundary conditions, and for the data points marked with open squares in the energy barrier curves.

and with the highest probability to occur.

V. DISCUSSION

Using (spin-polarized) scanning tunneling microscopy we have studied the magnetic properties of two different systems, namely Pd/Fe and Pd₂/Fe on Ir(111), in confined geometry. We find that the investigated islands host a variety of spin textures, including different metastable states. In islands with an effectively non-magnetic surrounding the spin texture exhibits a tilt at the edges. A strong hysteresis is observed in magnetic field dependent measurements where the virgin curve magnetic states are qualitatively different from the ones obtained when the magnetic field is subsequently applied in the opposite direction: whereas in the first case magnetic skyrmions are found, in the latter case the magnetic states are char-

acterized by branched 360° walls which end at island boundaries. When the surrounding of an island is ferromagnetic, such 360° walls perpendicular to island edges are avoided and target-like configurations can be found.

Using discrete spin simulations we can reproduce our experimental observations of multiple chiral configurations in small Pd/Fe islands. An analysis of the energy of chiral textures, which include the skyrmion, the target state and the 3π -skyrmion, indicates that these configurations can be stabilized from zero field up to different critical field magnitudes. Moreover, from the energy curves of these configurations as a function of the applied field, it can be inferred that the stability of some configurations can be explained by measuring the energy barriers separating them from energetically close configurations, for example a target state with a skyrmion. These results can be used as a reference for the observation of these magnetic states in future experiments. In particu-

lar, there is still a lack of experimental evidence of the 3π -skyrmion in a small confined system with interfacial DMI.

In order to reproduce different magnetic textures from SP-STM images of a field sweep experiment on Pd/Fe islands, we performed field sweep simulations in a range of field magnitudes smaller than the one used in the experiment and using specific initial states based on different numbers of skyrmions. Our simulation results showed multiple skyrmion-like domains trapped within branched spiral states that appear when inverting the field after crossing the zero magnitude, and we provided arguments to identify them by their topological number. The field magnitudes for the observation of chiral structures in our simulations differ from the ones in experiments because simulations are performed at zero temperature without any other external excitations such as the ones generated by the tunnel electrons in SP-STM. Accordingly, we did not exactly reproduce the results from the experiment, nonetheless it was still possible to stabilize most of the observed magnetic structures from the different field stages. Our simulations show that all the observed magnetic configurations should be accessible through an appropriate excitation of the system, thus further evidence of target states or 3π -skyrmions could be obtained in future experimental studies.

Using our simulations of a field sweep process it was not possible to obtain a target state from spiral configurations but mostly skyrmions from 360° domain walls at increasing strong field magnitudes (above 2 T) or large abrupt field changes. A possible solution to obtain these axially symmetric configurations with the field sweep method is specifying a suitable initial state, however this might be difficult in practice.

We performed a thorough analysis of skyrmions and target states under different conditions, by varying the size, applied field and boundary conditions of perfectly shaped hexagons. The main motivation for the modification of the boundary condition was the observation of a target-like state in the Pd₂/Fe islands on Ir(111), where the surrounding of the islands is ferromagnetic. Simulations of hexagonal islands of this material showed that for sufficiently small systems, skyrmions and target states in islands with a ferromagnetic rim have lower energy than the uniform state in a broader range of magnetic fields. In particular, for islands with radii around 8 nm, target states have lower energy than skyrmions when a ferromagnetic boundary is present.

In hexagons with free boundaries, we found that for radii up to approximately 8 nm and fields below 1.5 T, the tilting of spins at the island rim decreases the DMI energy and affects the skyrmion structure, by decreasing the skyrmion size in comparison to hexagons with a ferromagnetic rim. In contrast, due to the lack of canted spins at the island rim when ferromagnetic boundaries are present, skyrmions and target states are, in general, larger in size compared to hexagons with open boundaries. We observe that this larger size had an influ-

ence on the energy barriers separating a skyrmion from the ferromagnetic ordering and the target state from the skyrmion, making the barriers larger in systems with a ferromagnetic rim.

To gain an understanding of the ground state of the hexagon systems we computed a full phase diagram illustrating regions in hexagon radius and applied field space with the lowest energy configurations. We confirmed that spin spiral configurations are the ground states at weak fields and we identified regions where multiple $k\pi$ -skyrmion states are the lowest energy states at sufficiently large island sizes and applied fields. From the comparison of the energies of target states and skyrmions at hexagon sizes around 9 nm, we confirm that target states become the lowest energy states when a ferromagnetic rim is present, supporting our experimental observations of the favored stabilization of target states in Pd₂/Fe islands.

Furthermore, by analyzing minimum energy paths we found that in hexagons with free boundaries, up to fields of approximately 1.6 T and for hexagon circumradii above 4 nm, the minimum energy path between skyrmions and the uniform ordering is via the boundary, which is consistent with recent studies.³⁰⁻³² A ferromagnetic rim inhibits a skyrmion and a target state to escape through the boundary, hence forcing them to transition by a collapse or by a singularity. At weak fields and sufficiently large sizes these transitions have an energy barrier significantly larger than an escape mediated by the boundary when spins are not pinned at the island edges. Moreover, early results have shown that with free boundaries a target state can also transition at the boundary through spiral configurations. For instance, a lollipop-like state is formed when a target state reaches the sample edge and a single 360° wall emerges when half of the target state has escaped. These configurations are energetically favored at weak magnetic fields and as we saw in the simulated field sweep process, they tend to stabilize with branches perpendicular to the sample edges. These arguments indicate that skyrmions and target states should be more stable in islands with ferromagnetic boundaries since there is a larger energy cost for these structures to transition into other accessible states in the energy landscape. An accurate comparison of these solutions could be obtained in the future using effective magnitudes for the material parameters of Pd₂/Fe/Ir(111), for example, obtained from *ab initio* calculations.

VI. CONCLUSIONS

In summary, in this work we have employed discrete spin simulations to analyze experimental observations of skyrmionic textures in Pd/Fe and Pd₂/Fe islands on Ir(111). Our results show that discrete spin simulations can accurately explain our experimental findings. Furthermore, by modelling hexagonally shaped islands we

provide a more general understanding of how the applied field, system size and boundary conditions affect the stability of skyrmions and target states in confined geometries with interfacial DMI. In particular, we found that the presence of ferromagnetic boundaries favor the stability of target states in a region of applied field and island size that explains the experimental observation of a target-like state in Pd₂/Fe/Ir(111) islands. In addition, simulations predict conditions for the stability of novel magnetic configurations, such as $k\pi$ -skyrmions, that could be experimentally observed in the future.

We believe that the ease to carry out multiple computer simulated experiments can help for the future design of energy efficient spintronic devices based on small confined DMI systems, such as bit patterned recording media, where skyrmions or target states would encode

the memory bits.

VII. ACKNOWLEDGMENTS

We acknowledge financial support from CONICYT Chilean scholarship programme Becas Chile (72140061), the EPSRC Complex Systems Simulations DTC (EP/G03690X/1), the EPSRC Programme grant on Skyrmionics (EP/N032128/1), the Horizon 2020 European Research Infrastructure project OpenDreamKit (67 6541), and by the Deutsche Forschungsgemeinschaft (DFG, German Research Foundation) via SFB668-A8 and SPP2137.

The simulation data for a complete reproduction of this work can be found in Ref. 41.

-
- * d.cortes@soton.ac.uk
- ¹ A. N. Bogdanov, M. V. Kudinov, and D. A. Yablonskii, *Sov. Phys. Solid State*, *Sov. Phys. Solid State* **31**, 1707 (1989).
 - ² A. Bogdanov and D. Yablonskii, *Zh. Eksp. Teor. Fiz* **95**, 178 (1989).
 - ³ U. K. Rößler, A. N. Bogdanov, and C. Pfeleiderer, *Nature* **442**, 797 (2006).
 - ⁴ S. Mühlbauer, B. Binz, F. Jonietz, C. Pfeleiderer, A. Rosch, A. Neubauer, R. Georgii, and P. Böni, *Science* **323**, 915 (2009).
 - ⁵ S. Heinze, K. von Bergmann, M. Menzel, J. Brede, A. Kubetzka, R. Wiesendanger, and G. B. S. Blügel, *Nature Physics* **7**, 713 (2011).
 - ⁶ N. Romming, C. Hanneken, M. Menzel, J. E. Bickel, B. Wolter, K. von Bergmann, A. Kubetzka, and R. Wiesendanger, *Science* **341**, 636 (2013).
 - ⁷ N. Romming, A. Kubetzka, C. Hanneken, K. von Bergmann, and R. Wiesendanger, *Physical Review Letters* **114**, 1 (2015).
 - ⁸ R. Wiesendanger, *Nature Reviews Materials* **1**, 16044 (2016).
 - ⁹ A. Bogdanov and A. Hubert, *Journal of magnetism and magnetic materials* **138**, 255 (1994).
 - ¹⁰ A. Bogdanov and A. Hubert, *Journal of Magnetism and Magnetic Materials* **195**, 182 (1999).
 - ¹¹ S. Rohart and A. Thiaville, *Physical Review B* **88**, 184422 (2013).
 - ¹² A. O. Leonov, U. K. Rößler, and M. Mostovoy, in *EPJ Web of Conferences*, Vol. 75 (EDP Sciences, 2014) p. 05002.
 - ¹³ M. Beg, R. Carey, W. Wang, D. Cortés-Ortuño, M. Vousden, M.-A. Bisotti, M. Albert, D. Chernyshenko, O. Hovorka, R. L. Stamps, and H. Fangohr, *Scientific Reports* **5**, 17137 (2015).
 - ¹⁴ Y. Liu, H. Du, M. Jia, and A. Du, *Physical Review B* **91**, 094425 (2015).
 - ¹⁵ R. Carey, M. Beg, M. Albert, M.-A. Bisotti, D. Cortés-Ortuño, M. Vousden, W. Wang, O. Hovorka, and H. Fangohr, *Applied Physics Letters* **109**, 122401 (2016).
 - ¹⁶ A. G. Kolesnikov, M. E. Stebliy, A. S. Samardak, and A. V. Ognev, *Scientific Reports* **8**, 16966 (2018).
 - ¹⁷ J. Hagemeister, A. Siemens, L. Rózsa, E. Y. Vedmedenko, and R. Wiesendanger, *Physical Review B* **97**, 174436 (2018).
 - ¹⁸ M. Shen, Y. Zhang, J. Ou-Yang, X. Yang, and L. You, *Applied Physics Letters* **112**, 062403 (2018).
 - ¹⁹ S. Li, J. Xia, X. Zhang, M. Ezawa, W. Kang, X. Liu, Y. Zhou, and W. Zhao, *Applied Physics Letters* **112**, 142404 (2018).
 - ²⁰ S. Komineas and N. Papanicolaou, *Physical Review B* **92**, 064412 (2015).
 - ²¹ S. Komineas and N. Papanicolaou, *Physical Review B* **92**, 174405 (2015).
 - ²² X. Zhang, J. Xia, Y. Zhou, D. Wang, X. Liu, W. Zhao, and M. Ezawa, *Physical Review B* **94**, 094420 (2016).
 - ²³ N. Nagaosa and Y. Tokura, *Nature nanotechnology* **8**, 899 (2013).
 - ²⁴ M. Finazzi, M. Savoini, a. R. Khorsand, a. Tsukamoto, a. Itoh, L. Duò, a. Kirilyuk, T. Rasing, and M. Ezawa, *Physical Review Letters* **110**, 177205 (2013).
 - ²⁵ S. Zhang, F. Kronast, G. van der Laan, and T. Hesjedal, *Nano Letters* **18**, 1057 (2018).
 - ²⁶ F. Zheng, H. Li, S. Wang, D. Song, C. Jin, W. Wei, A. Kovács, J. Zang, M. Tian, Y. Zhang, H. Du, and R. E. Dunin-Borkowski, *Phys. Rev. Lett.* **119**, 197205 (2017).
 - ²⁷ C. Jin, Z.-A. Li, A. Kovács, J. Caron, F. Zheng, F. N. Rybakov, N. S. Kiselev, H. Du, S. Blügel, M. Tian, *et al.*, *Nature Communications* **8** (2017), doi:10.1038/ncomms15569.
 - ²⁸ A. Fert, N. Reyren, and V. Cros, *Nature Reviews Materials* **2**, 1 (2017).
 - ²⁹ P. F. Bessarab, V. M. Uzdin, and H. Jónsson, *Computer Physics Communications* **196**, 1 (2015).
 - ³⁰ D. Cortés-Ortuño, W. Wang, M. Beg, R. A. Pepper, M.-A. Bisotti, R. Carey, M. Vousden, T. Kluyver, O. Hovorka, and H. Fangohr, *Scientific Reports* **7**, 4060 (2017).
 - ³¹ D. Stosic, J. Mulkers, B. Van Waeyenberge, T. B. Luder-mir, and M. V. Milošević, *Physical Review B* **95**, 214418 (2017).
 - ³² P. F. Bessarab, G. P. Müller, I. S. Lobanov, F. N. Rybakov, N. S. Kiselev, H. Jónsson, V. M. Uzdin, S. Blügel, L. Bergqvist, and A. Delin, *Scientific Reports* **8**, 3433 (2018).
 - ³³ R. Wiesendanger, *Rev. Mod. Phys.* **81**, 1495 (2009).

- ³⁴ C. Hanneken, F. Otte, A. Kubetzka, B. Dupé, N. Romming, K. von Bergmann, R. Wiesendanger, and S. Heinze, *Nature Nanotechnology* **10**, 1039 (2015).
- ³⁵ M.-A. Bisotti, D. Cortés-Ortuño, R. Pepper, W. Wang, M. Beg, T. Kluyver, and H. Fangohr, *Journal of Open Research Software* **6**, 22 (2018).
- ³⁶ A. O. Leonov, T. L. Monchesky, N. Romming, A. Kubetzka, A. N. Bogdanov, and R. Wiesendanger, *New Journal of Physics* **18**, 1 (2015).
- ³⁷ I. S. Lobanov, H. Jónsson, and V. M. Uzdin, *Physcal Review B* **94**, 174418 (2016).
- ³⁸ S. von Malottki, B. Dupé, P. F. Bessarab, A. Delin, and S. Heinze, *Scientific Reports* **7**, 12299 (2017).
- ³⁹ N. S. Kiselev, A. N. Bogdanov, R. Schäfer, and U. K. Röbber, *Journal of Physics D: Applied Physics* **44**, 392001 (2011).
- ⁴⁰ P.-J. Hsu, A. Kubetzka, A. Finco, N. Romming, K. von Bergmann, and R. Wiesendanger, *Nature Nanotechnology* **12**, 123 (2016).
- ⁴¹ D. Cortés-Ortuño, N. Romming, M. Beg, K. von Bergmann, R. Wiesendanger, H. Fangohr, and A. Kubetzka, “Data set for: Stability of chiral magnetic configurations in iron palladium islands,” Zenodo doi:10.5281/zenodo.1438396. Github: https://github.com/davidcortesortuno/paper-2018_stability_pdfeir_islands (2018).